# Chemiluminescence- and machine learning-based monitoring of premixed ammonia-methane-air flames

Thibault F Guiberti, Nader N Shohdy, Santiago Cardona, Xuren Zhu, Laurent Selle, Corentin J Lapeyre

▶ **To cite this version:**

Thibault F Guiberti, Nader N Shohdy, Santiago Cardona, Xuren Zhu, Laurent Selle, et al.. Chemiluminescence- and machine learning-based monitoring of premixed ammonia-methane-air flames. Applications in Energy and Combustion Science, 2023, 16, pp.100212. 10.1016/j.jaecs.2023.100212 . hal-04532070

**HAL Id: hal-04532070**

**https://ut3-toulouseinp.hal.science/hal-04532070v1**

Submitted on 4 Apr 2024

**HAL** is a multi-disciplinary open access archive for the deposit and dissemination of scientific research documents, whether they are published or not. The documents may come from teaching and research institutions in France or abroad, or from public or private research centers.

L'archive ouverte pluridisciplinaire **HAL**, est destinée au dépôt et à la diffusion de documents scientifiques de niveau recherche, publiés ou non, émanant des établissements d'enseignement et de recherche français ou étrangers, des laboratoires publics ou privés.

Distributed under a Creative Commons Attribution - NonCommercial - NoDerivatives 4.0 International License

Applications in Energy and Combustion Science 16 (2023) 100212

Contents lists available at ScienceDirect

Applications in Energy and Combustion Science

journal homepage: www.sciencedirect.com/journal/applications-in-energy-and-combustion-science

# Chemiluminescence- and machine learning-based monitoring of premixed ammonia-methane-air flames

Thibault F. Guiberti [a,b,*], Nader N. Shohdy [a,b], Santiago Cardona [a], Xuren Zhu [a], Laurent Selle [c], Corentin J. Lapeyre [d]

[a] Clean Combustion Research Center, King Abdullah University of Science and Technology (KAUST), Thuwal 23955-6900, Kingdom of Saudi Arabia
[b] Mechanical Engineering Program, Physical Science and Engineering Division, King Abdullah University of Science and Technology
[c] Institut de Mécanique des Fluides de Toulouse, IMFT, Université de Toulouse, CNRS, Toulouse, France
[d] CERFACS, 42 Avenue Gaspard Coriolis, Toulouse, France

ARTICLE INFO

*Keywords:*
Spontaneous emission
Gaussian process regression
AI
Swirl flame
Twin flame
Flame sensor

ABSTRACT

This work presents the development and validation of an algorithm capable of predicting the equivalence ratio and the ammonia fraction of premixed ammonia-methane-air flames using only measured OH*, NH*, CN*, and CH* chemiluminescence intensities as input. This machine learning algorithm relies on Gaussian process regression (GPR). It was trained and validated with data previously recorded in laminar flames, and it was then tested with new data recorded in more practical, turbulent swirl flames. The algorithm performs well for laminar and turbulent flames for wide ranges of equivalence ratio ($0.80 \leq \phi \leq 1.20$) and ammonia fraction ($0 \leq X_{NH3} \leq 0.60$). For turbulent swirl flames, the prediction errors in the equivalence ratio and on the ammonia fraction are smaller than 0.05, except for a very small subset of operating conditions where the error is up to 0.10. Additional tests were performed by adding NO* and $CO_2$* to the list of inputs, but this did not improve the predictions. The GPR algorithm was then benchmarked against linear and polynomial regressions and a more conventional way of inferring flame properties from chemiluminescence measurements, namely the ratio-based method. This method relies only on CN*/NO* and NH*/CH* ratios to predict the equivalence ratio and the ammonia fraction. Its prediction errors were often larger than 0.15, which is significantly worse than that of the GPR algorithm. Consequently, this work constitutes a solid basis for the future development of non-intrusive sensors to monitor practical ammonia-methane-air flames.

## 1. Introduction

Research on ammonia flames is accumulating a lot of momentum (see for example review articles [1–6]) and there is little doubt that the deployment of practical devices fueled with ammonia for power and mobility applications is forthcoming [7–9]. As a first step towards total decarbonization, or to offset ammonia's weak reactivity [1], blends of ammonia and conventional hydrocarbons such as methane are likely to be used in some applications (see for example [10–16]). Previous research established that the low flame speed and the propensity to emit nitrogen oxides (NOx) are two potential issues that need to be addressed in combustors fueled with ammonia-methane blends [1,4,8,13,17-22]. For premixed flames, data from these studies and many others show that the equivalence ratio and the ammonia fraction are first-order parameters for flame speed and NOx emissions. Consequently, sensors capable of monitoring the equivalence ratio and the ammonia fraction in premixed ammonia-methane-air flames are desirable.

To avoid intrusiveness and to allow implementation in practical systems with limited optical access, chemiluminescence-based optical sensors may be used. Previous research showed that chemiluminescence can be recorded and analyzed to infer important flame properties. For example, the ratio of OH* to CH* chemiluminescence intensities is a suitable surrogate for the equivalence ratio in methane-air flames (e.g., [23–28]). In biogas-air flames [29,30], the OH*/$CO_2$* ratio informs on the $CO_2$ concentration and the formation of nitrogen oxide can be detected in flames that burn nitrogen compounds such as ammonia by monitoring the chemiluminescence intensities of NH* or CN* [31]. There are many more examples of applications of chemiluminescence in

* Corresponding author at: Clean Combustion Research Center, 4276, Al-Kindi West (building 5), King Abdullah University of Science and Technology, Thuwal 23955-6900, Saudi Arabia.
*E-mail address:* thibault.guiberti@kaust.edu.sa (T.F. Guiberti).

https://doi.org/10.1016/j.jaecs.2023.100212
Received 15 April 2023; Received in revised form 8 September 2023; Accepted 28 September 2023
Available online 29 September 2023
2666-352X/© 2023 The Authors. Published by Elsevier Ltd. This is an open access article under the CC BY-NC-ND license (http://creativecommons.org/licenses/by-nc-nd/4.0/).

lab-scale or practical flames, but they cannot be all listed here. Studies published before 2010 are reviewed in [28].

For premixed ammonia-methane-air flames, Zhu et al. [32] measured the chemiluminescence spectrum between 200 and 450 nm for wide ranges of equivalence ratio and ammonia fraction and highlighted the potential of chemiluminescence to monitor such flames (for simplicity, the light spontaneously emitted by the flame is here called *chemiluminescence*, even though a fraction of the excited radicals can be formed via thermal excitation). This potential comes from the large number of excited radicals that are active in this spectral range, namely NO*, OH*, NH*, CN*, $CO_2$*, and CH*. The chemiluminescence of flames featuring ammonia in the fuel blend was also explored in [19,33-44] among others. Fig. 1, adapted from [32], shows the chemiluminescence intensity measured for these six excited radicals as a function of the equivalence ratio ($\phi$) for different ammonia fractions ($X_{NH3}$). Measurements were made in laminar twin flames stabilized with a counterflow burner (strain rate of $a = 150$ /s), and the chemiluminescence signal was spatially integrated across the flame. The chemiluminescence intensity depends on the equivalence ratio and the ammonia fraction for all six excited radicals, and the trends are quantitatively different. The curves of the chemiluminescence intensity vs. equivalence ratio are all bell-shaped, but the equivalence ratio at the peak varies with the excited radical and ammonia fraction. The trend of chemiluminescence intensity vs. ammonia fraction is monotonic for OH*, $CO_2$* and CH*, but it is non-monotonic for NO*, NH*, and CN*.

After testing all possible ratios of two excited radicals, Zhu et al. [32] found that CN*/OH* and CN*/NO* ratios are possible surrogates for the equivalence ratio and that the NH*/CH* ratio can be used to infer the ammonia fraction. However, these ratios are only useful in specific ranges of equivalence ratio and ammonia fraction, and they provide a level of accuracy that may be insufficient in some applications. In [32], the analysis was only made with ratios of two excited radicals, which is a small subset of possible surrogates.

More complex approaches that combine multiple spectral contributions to predict relevant flame properties have been tested in methane-air and methane-hydrogen-air flames [45–48]. The earliest effort that

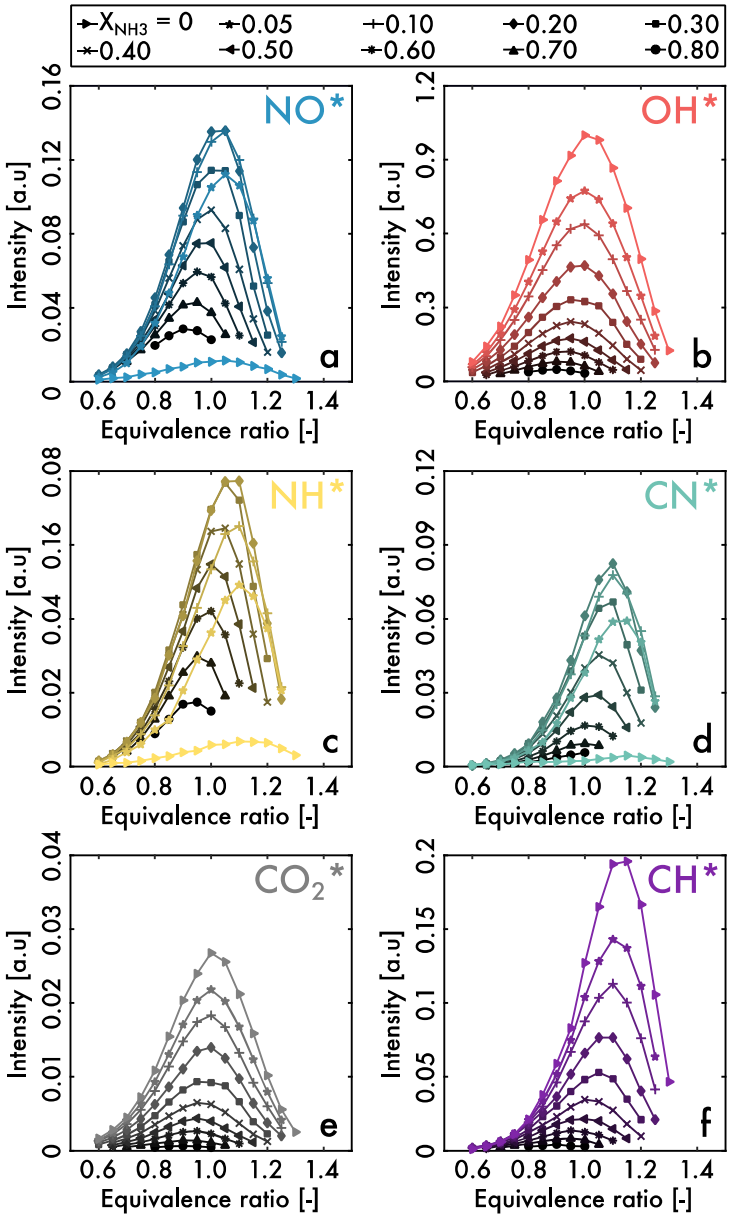


**Fig. 1.** Measured chemiluminescence intensities as a function of the equivalence ratio for different ammonia fractions in premixed laminar twin flames. Adapted from [32].

the authors are aware of is that of Ballester et al. [45] who successfully inferred the hydrogen fraction, the equivalence ratio, and NOx and CO emissions in premixed methane-hydrogen flames using chemiluminescence and an artificial neural network (ANN). Later, Tripathi et al. [46] showed that it is also possible to accurately infer the equivalence ratio of premixed methane-air flames using chemiluminescence in the 250 to 650 nm range along with a partial least-square regression approach. Using proper orthogonal decomposition (POD) of chemiluminescence spectra followed by a reduced-order model employing the kriging method, Yoon et al. [47] achieved yet a better prediction of equivalence ratio, as well as of pressure. The useful properties of this method are that the most important spectral features are automatically extracted, and that minimal calibration is required.

To the best of the authors' knowledge, these types of chemiluminescence- and machine learning-based methods were never tested in premixed ammonia-methane-air flames for which the chemiluminescent signature is much richer. This is the scope of the present study. The two main objectives are:

1 Demonstrate that machine learning regression can uncover complex but useful relationships between the chemiluminescence intensities from the six excited radicals and the equivalence ratio and/or the ammonia fraction.
2 Verify if these relationships can be generalized to turbulent swirl flames that are more representative of practical flames.

## 2. Methods

### 2.1. Machine learning regression

In this study, a Gaussian Process Regression (GPR) algorithm [49] was used to predict the equivalence ratio and the ammonia fraction of ammonia-methane-air flames using chemiluminescence intensities of the NO*, OH*, NH*, CN*, $CO_2$*, and CH* excited radicals. To train and validate this supervised machine learning algorithm, the data recorded by Zhu et al. [32] in laminar twin flames were used. The spatially integrated chemiluminescence intensities measured in [32] were already normalized, which typically helps convergence and improves accuracy. Data were further pre-processed for the present study by taking the ratio X*/OH*, where X* refers to NO*, NH*, CN*, $CO_2$*, or CH*. Ratios are needed to cancel effects of the flame surface area and, in turn, enable the application of the algorithm to other flame geometries (see Section 3.3). Excited radical OH* was chosen for normalization because it is the only measured excited radical that is present in significant quantities in all flames of interest, namely ammonia-methane-air, methane-air, or ammonia-air flames. Therefore, the GPR algorithm features up to five inputs (any combination of NO*/OH*, NH*/OH*, CN*/OH*, $CO_2$*/OH*, and CH*/OH*) and two outputs ($\phi$ and $X_{NH3}$).

The dataset from [32] includes 214 data points, corresponding to wide ranges of equivalence ratio ($0.60 \leq \phi \leq 1.30$), ammonia fraction ($0 \leq X_{NH3} \leq 0.80$), and strain rate ($80 \leq a \leq 300$ /s). GPR is well suited to datasets of this dimensionality and size. In addition, GPR is probabilistic by design, meaning that it supposes that the true value is normally distributed about the mean predicted value. Therefore, it provides an estimate of the corresponding standard deviation, which can be used to infer the confidence interval for its predictions. Note that other types of machine learning regression methods exist, but those tested by the authors (e.g., ordinary least squares and lasso linear regression or support vector machines regression) did not perform as well as GPR for this application.

The GPR algorithm was implemented in scikit-learn [50], an open-source library of machine learning tools based on the Python programming language. Application of GPR requires specifying a covariance kernel function, and the scikit-learn library includes numerous options. After multiple tests, the rational quadratic kernel was found to be a suitable option for the present dataset. It is simply parameterized by a length-scale hyperparameter $l$ and a scale mixture hyperparameter α that can be varied and optimized using functions built in scikit-learn to achieve the right balance between underfitting and overfitting. The rational quadratic kernel $k_{rq}$ is given by:

$$k_{rq}(x_i,\ x_j) = \left(1 + \frac{d(x_i,\ x_j)^2}{2\alpha l^2}\right)^{-\alpha} \quad (1)$$

where $x_i$ and $x_j$ are datapoints and $d(x_i,\ x_j)$ is the Euclidean distance between these datapoints. In GPR, multiple kernels can be combined by addition or by multiplication. Here, to improve numerical stability, a white kernel $k_w$ was simply added to the rational quadratic kernel to yield $k = k_{rq} + k_w$. The white kernel is only parametrized by a noise level $n$ as follows:

$$k_w(x_i,\ x_j) = n \text{ if } x_i = x_j \text{ else } 0 \quad (2)$$

Similar performance was found using a Matern kernel instead of a rational quadratic kernel, and both the rational quadratic and Matern kernels slightly overperformed a radial basis kernel. The reader is referred to [51] for more details about GPR.

To train the GPR algorithm, 75% of the dataset was used, corresponding to 160 data points. The 160 data points were randomly assigned by the *train_test_split* function built in scikit-learn after a seed number was prescribed. Different seed numbers were used to assess the universality of the optimized hyperparameters (see Section 3.1). The GPR algorithm was extended to also include the possibility to introduce random error into the dataset, which was used to quantify the robustness of the method to the uncertainty of chemiluminescence intensity measurements (see Section 3.4). The quality of the regression for any given sets of hyperparameters and inputs was quantified by the coefficient of determination $R^2$ of the regression, applied to the validation dataset, i.e., the remaining 54 (25%) data points from Zhu et al. [32].

Once the hyperparameters and inputs were optimized, the performance of the prediction of equivalence ratio and ammonia fraction by the GPR algorithm was quantified using a test dataset that was not used for training or validation. The test dataset was gathered via measurements of chemiluminescence in premixed turbulent swirl ammonia-methane-air flames, which were conducted specifically for this study. These measurements are detailed in Section 3.3.

The GPR algorithm, including the data reading and pre-processing, regression, and plotting sections, is available as supplementary material. The training, validation, and test datasets are also available as supplementary material.

### 2.2. Experimental setup

To collect the test dataset, the chemiluminescence spectra of premixed, turbulent swirl, ammonia-methane-air flames were recorded at atmospheric pressure. These flames were stabilized in a generic, lab-scale burner (cf. Fig. 2) similar to that used and described in detail in [52–54]. A perfectly premixed mixture of ammonia, methane, and air was supplied to the plenum of the burner and was then fed in a radial swirler through a converging nozzle. The swirl number was $S = 0.4$. The reactants then flowed into a cylindrical combustion chamber made of quartz (70 mm in diameter and 200 mm in length) through an 18-mm diameter nozzle. Different equivalence ratios ($0.80 \leq \phi \leq 1.20$) and ammonia fractions ($0 \leq X_{NH3} \leq 0.60$) were tested, and the bulk velocity through the nozzle was set to 5 m/s. The 29 different conditions that were tested corresponded to slightly different bulk Reynolds numbers, but these were always in the order of $Re \approx 6000$. The corresponding thermal powers varied between $P = 2.5$ and 4.8 kW.

The gas mass flow rates were prescribed with digital mass flow controllers (Bronkhorst EL-FLOW F-200 series) that were calibrated in-house with gas flow calibrators (MesaLabs FlexCal series). This led to

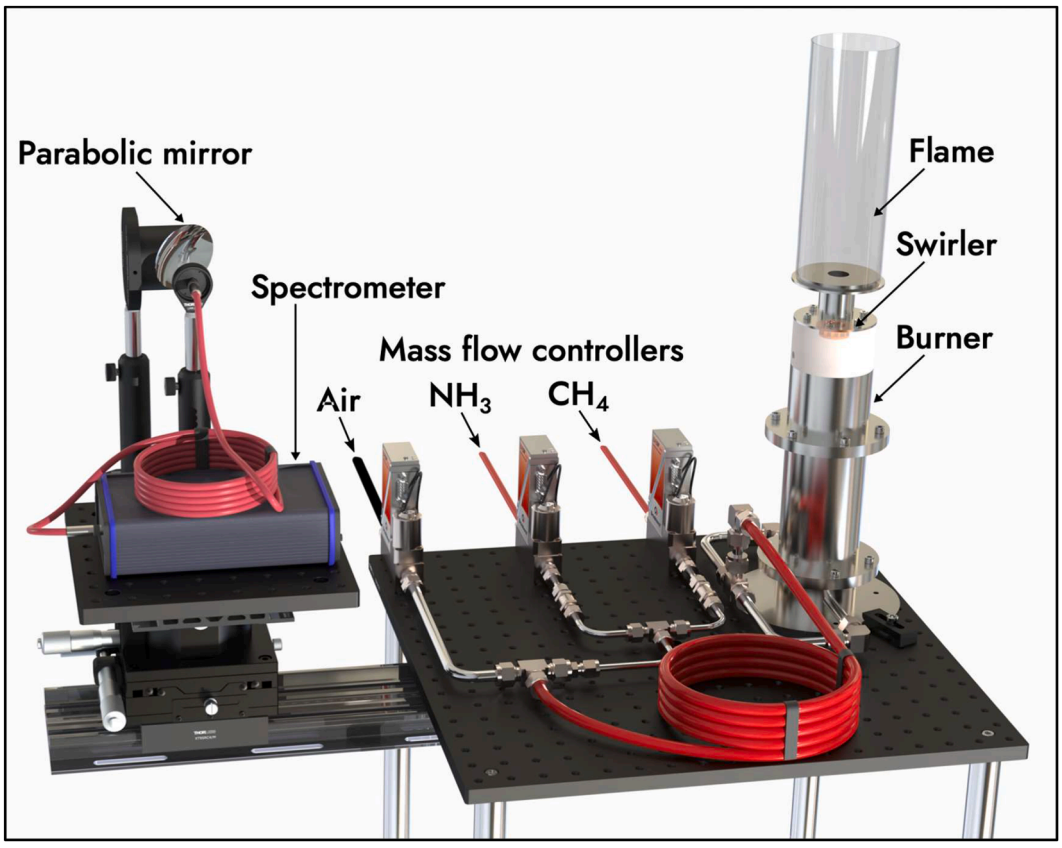


**Fig. 2.** Schematic of the experimental setup.

an accuracy better than 1% for each flow rate and, in turn, to maximum errors in prescribing equivalence ratio, ammonia fraction, and bulk velocity of 2, 2, and 1%, respectively. The gasses were mixed rapidly downstream of the mass flow controllers and were allowed to fully mix while flowing through a 3-m long, 9.5-mm diameter plastic tube before entering the burner's plenum.

The time-average spectrum of flame chemiluminescence was recorded for the 29 operating conditions with a UV-capable, bench spectrometer (Avantes AvaSpec-ULS3648), also shown in Fig. 2. Light emitted by the flame was collected with a 50.8-mm diameter, 50.8-mm focal distance, UV-enhanced, off-axis parabolic mirror (Thorlabs MPD229-F01). This parabolic mirror was mounted 500-mm away from the flame, corresponding to roughly 10× its focal distance, which allowed to focus the light emitted by the flame into the 400-μm core of an optical fiber (Avantes FC-UVIR400–2). A mirror was chosen instead of a lens to collect and focus the light because of its achromatic nature. Although some of the flames were slightly taller than 50.8 mm, this strategy allowed to accumulate light from almost all regions of the flame. The spectrometer had a spectral resolution of 0.7 nm and its X- and Y-axes were calibrated with a mercury lamp (Teledyne Intellical) and a deuterium lamp (Hamamatsu L6565), respectively. The spectrometer's integration time was set to 9 s in all cases and each spectrum was the average of 10 replicates.

Fig. 3 shows an example of the chemiluminescence spectrum between 220 and 450 nm measured for $\phi = 1.0$ and $X_{NH3} = 0.50$. Contributions from the six most active excited radicals, namely NO*, OH*, NH*, CN*, $CO_2$*, and CH*, are clearly visible. Like in [32,42,43], the broadband background was determined using anchor points (orange circles in Fig. 3) and interpolations (orange dashed lines in Fig. 3) so that contributions attributed only to specific excited radicals could be quantified. To obtain the chemiluminescence intensity from each radical and for each operating condition, the background-removed spectrum

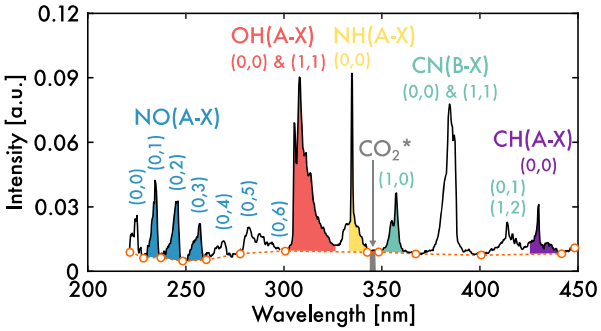


**Fig. 3.** Chemiluminescence spectrum measured in a premixed swirl ammonia-methane-air flame with $\phi = 1.0$ and $X_{NH3} = 0.50$. Color labels show features assignment to different excited radicals, electronic transitions, and vibrational bands. The orange dashed line show the broadband background interpolated between anchor points (orange circles). Colors show the spectral bands over which the contribution from each excited radical is integrated to obtain its chemiluminescence intensity.

was integrated over a specific range, as shown by the different colors in Fig. 3. For each radical, the spectral range for integration was chosen to avoid interference between species, and the reader is referred to [32] for more details. Ranges are similar but not strictly identical to those chosen to post-process spectra in [32] because the spectrometer used in this study is different and it features a slightly different spectral resolution. Using the chemiluminescence intensity for each excited radical X*, the ratio X*/OH* is then obtained.

## 3. Results and discussion

### 3.1. Training and validation of the GPR algorithm with laminar flames

Fig. 4 shows the equivalence ratio (a) and the ammonia fraction (b) predicted by the GPR algorithm as a function of their true values after the algorithm was trained with 75% of the laminar flame data from Zhu et al. [32]. All excited radicals were used, leading to 5 inputs. The blue squares correspond to the 160 training data points, and the red circles represent the 54 validation data points. For the equivalence ratio, the coefficient of determination for the regression on the validation data points is $R^2 = 0.990$, suggesting that the prediction was successful. A similar level of performance was obtained for the ammonia fraction, with $R^2 = 0.993$. To achieve this, the optimum GPR hyperparameters were $l = 0.51$, $\alpha = 0.15$, and $n = 2.3 \times 10^{-4}$ for the equivalence ratio and $l = 0.29$, $\alpha = 3.00$, and $n = 1.0 \times 10^{-4}$ for the ammonia fraction. Even though hyperparameters are the result of an automatic optimization by the GPR algorithm, it is useful to verify if their values are reasonable considering the data at hand. From Eq. (1), it is seen that the length scale $l$ is used to normalize the Euclidian distance between datapoints $d$. Therefore, a value $l = 0.51$ is consistent with values of excited radical ratios that span between 0.002 and 0.656. Authors are not aware of any limitations or guidelines regarding the value of the mixture scale hyperparameters $\alpha$. The white noise of level $n$ acts as a numerical stabilizer and its optimal value is hard to relate to the input data using physical arguments. However, one may take comfort in noticing that a value $n = 2.3 \times 10^{-4}$ is much smaller than potential measurements errors (on the order of $1 \times 10^{-2}$) on the output data with which it shares dimensions, namely equivalence ratio or ammonia fraction. This confirms that injection of noise only serves its purpose of numerical stabilizer instead of also somewhat compensating for variability due to potential measurements errors.

For Fig. 4, training and validation were achieved with a random assignment of the respective 160 and 54 data points and it is useful to examine how different the prediction's performance would be for a different assignment. This was achieved by trying 100 other seed numbers in scikit-learn's *train_test_split* function while keeping the same hyperparameters. The mean, coefficient of variation (COV), minimum, and maximum values of the regression coefficients are shown in Table 1. The coefficients of variation are below 0.5% for the equivalence ratio and for the ammonia fraction, which suggests that the regression's performance is not very sensitive to the choice of the training dataset.

**Table 1**
Mean, coefficient of variation (COV), minimum, and maximum values of the coefficient of regression $R^2$ for hyperparameters $l = 0.51$, $\alpha = 0.15$, and $n = 2.3 \times 10^{-4}$ (equivalence ratio) and $l = 0.29$, $\alpha = 3.00$, and $n = 1.0 \times 10^{-4}$ (ammonia fraction) if all excited radicals are used as inputs (i.e., inputs are NO*/OH*, NH*/OH*, CN*/OH*, $CO_2$*/OH*, and CH*/OH*).

| | Mean $R^2$ | COV $R^2$ | Min $R^2$ | Max $R^2$ |
|---|---|---|---|---|
| $\phi$ | 0.992 | 0.4% | 0.980 | 0.998 |
| $X_{NH3}$ | 0.996 | 0.2% | 0.991 | 0.999 |

### 3.2. Optimization of the inputs

Initially, all six excited radicals were used as inputs for the GPR algorithm. This means that, to use this algorithm for equivalence ratio and ammonia fraction predictions, all six exited radicals must be measured, which could be impractical or too expensive in some applications. Therefore, the GPR algorithm was also trained and challenged with a reduced number of inputs/excited radicals. Fig. 5 shows the equivalence ratio (a) and the ammonia fraction (b) predicted by the GPR algorithm as a function of their true values if the NO* excited radical is excluded, i.e., if the NO*/OH* ratio is no longer used as an input, leading to 4 inputs. The NO* excited radical was excluded first because its contribution to the chemiluminescence spectrum is the deepest in the UV, meaning that it is the hardest to measure. Figs. 4 and 5 are very similar, and only the coefficient of determination of the regression on equivalence ratio is marginally degraded if NO* is excluded. The optimal hyperparameters are different if NO* is excluded: $l = 0.40$, $\alpha = 0.29$, and $n = 2.9 \times 10^{-4}$ for the equivalence ratio and $l = 0.24$, $\alpha = 0.74$, and $n = 1.0 \times 10^{-4}$ for the ammonia fraction. Table 2 shows the corresponding $R^2$ statistics for the 100 different seed numbers of the training dataset.

Based on Figs. 4 and 5 and Tables 1 and 2, it is concluded that removing NO* from the inputs does not lead to significant degradation of the GPR algorithm's performance, yet it reduces the complexity and cost of the associated measurements.

Fig. 6 shows the prediction by the GPR algorithm if the NO* and $CO_2$* excited radicals are both excluded, leading to 3 inputs. Indeed, Fig. 1 shows that trends of $CO_2$* with equivalence ratio and ammonia fraction are similar to those of OH*, suggesting that $CO_2$* information could be redundant. Again, Fig. 6 is hardly distinguishable from Figs. 4 and 5, meaning that removing both NO* and $CO_2$* from the inputs does not significantly degrade the GPR algorithm's prediction performance. The optimal hyperparameters if NO* and $CO_2$* are excluded are $l = 0.39$, $\alpha = 0.30$, and $n = 3.0 \times 10^{-4}$ for the equivalence ratio and $l = 0.27$, $\alpha = 0.55$, and $n = 1.3 \times 10^{-4}$ for the ammonia fraction. Table 3 shows the corresponding $R^2$ statistics for the 100 different training dataset seed

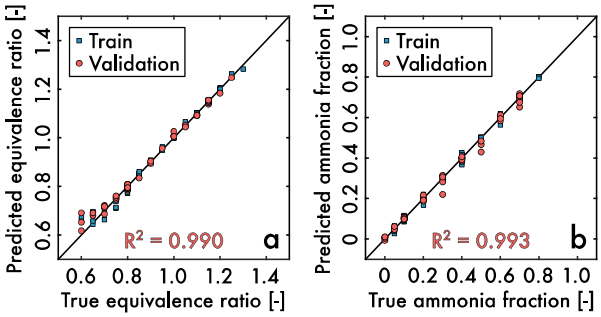


**Fig. 4.** Predicted equivalence ratio (a) and ammonia fraction (b) as a function of their true values for the training (blue squares) and validation (red circles) data points and for the optimum hyperparameters $l = 0.51$, $\alpha = 0.15$, and $n = 2.3 \times 10^{-4}$ (equivalence ratio) and $l = 0.29$, $\alpha = 3.00$, and $n = 1.0 \times 10^{-4}$ (ammonia fraction). All excited radicals were used as inputs (i.e., inputs are NO*/OH*, NH*/OH*, CN*/OH*, $CO_2$*/OH*, and CH*/OH*). Coefficients of determination in red correspond to the regressions on the validation data points.

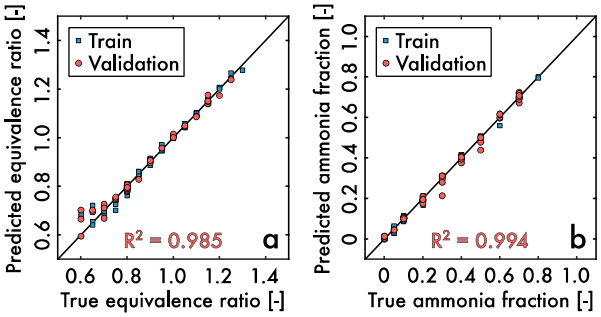


**Fig. 5.** Predicted equivalence ratio (a) and ammonia fraction (b) as a function of their true values for the training (blue squares) and validation (red circles) data points and for the optimum hyperparameters $l = 0.40$, $\alpha = 0.29$, and $n = 2.9 \times 10^{-4}$ (equivalence ratio) and $l = 0.24$, $\alpha = 0.74$, and $n = 1.0 \times 10^{-4}$ (ammonia fraction). The NO* excited radical was excluded from the inputs (i.e., inputs are NH*/OH*, CN*/OH*, $CO_2$*/OH*, and CH*/OH*). Coefficients of determination in red correspond to the regressions on the validation data points.

**Table 2**
Mean, coefficient of variation (COV), minimum, and maximum values of the coefficient of regression $R^2$ for hyperparameters $l = 0.40$, $\alpha = 0.29$, and $n = 2.9 \times 10^{-4}$ (equivalence ratio) and $l = 0.24$, $\alpha = 0.74$, and $n = 1.0 \times 10^{-4}$ (ammonia fraction) if NO* is excluded from the inputs (i.e., inputs are NH*/OH*, CN*/OH*, $CO_2$*/OH*, and CH*/OH*).

| | Mean $R^2$ | COV $R^2$ | Min $R^2$ | Max $R^2$ |
|---|---|---|---|---|
| $\phi$ | 0.989 | 0.4% | 0.976 | 0.996 |
| $X_{NH3}$ | 0.996 | 0.2% | 0.988 | 0.999 |

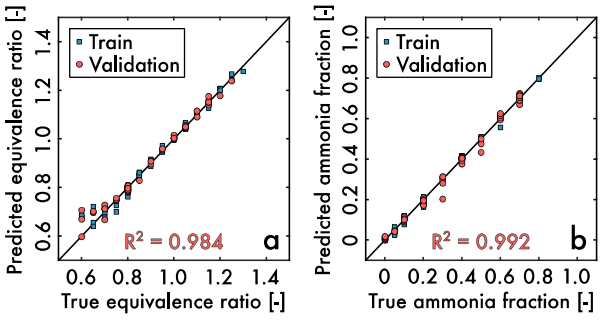


**Fig. 6.** Predicted equivalence ratio (a) and ammonia fraction (b) as a function of their true values for the training (blue squares) and validation (red circles) data points and for the optimum hyperparameters $l = 0.39$, $\alpha = 0.30$, and $n = 3.0 \times 10^{-4}$ (equivalence ratio) and $l = 0.27$, $\alpha = 0.55$, and $n = 1.3 \times 10^{-4}$ (ammonia fraction). The NO* and $CO_2$* excited radicals were excluded from the inputs (i.e., inputs are NH*/OH*, CN*/OH*, and CH*/OH*). Coefficients of determination in red correspond to the regressions on the validation data points.

**Table 3**
Mean, coefficient of variation (COV), minimum, and maximum values of the coefficient of regression $R^2$ for hyperparameters $l = 0.39$, $\alpha = 0.30$, and $n = 3.0 \times 10^{-4}$ (equivalence ratio) and $l = 0.27$, $\alpha = 0.55$, and $n = 1.3 \times 10^{-4}$ (ammonia fraction) if NO* and $CO_2$* are excluded from the inputs (i.e., inputs are NH*/OH*, CN*/OH*, and CH*/OH*).

| | Mean $R^2$ | COV $R^2$ | Min $R^2$ | Max $R^2$ |
|---|---|---|---|---|
| $\phi$ | 0.988 | 0.4% | 0.976 | 0.995 |
| $X_{NH3}$ | 0.995 | 0.2% | 0.991 | 0.998 |

numbers.

A similar excercise was performed by further excluding the remaining excited radicals, one by one. It was found that excluding any

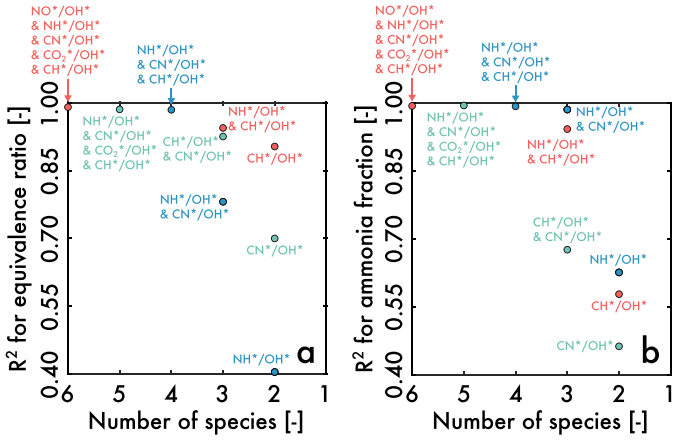


**Fig. 7.** Coefficients of determination of the regression on the validation data points as a function of the number of excited radicals used as inputs.

of the OH*, NH*, CN*, or CH* radicals leads to significant degradation of the GPR algorithm's prediction performance. This is shown in Fig. 7 that plots the coefficients of regression obtained with optimal hyperparameters as a function of the number of species used as inputs. When three species are considered, i.e., two ratios are used as inputs, the coefficients of regression are noticeably smaller than those obtained if only NO* and $CO_2$* are excluded from the inputs. Perhaps the only exception is the combination of excited radicals OH*, NH*, and CN* that exhibits a good prediction of the ammonia fraction. However, this combination predicts equivalence ratio poorly. No combination of two excited radicals yields satisfying predictions. Therefore, the preferred algorithm for this application was found to be the one trained with three inputs, i.e., four excited radicals, specifically NH*/OH*, CN*/OH*, and CH*/OH* with the following hyperparameters: $l = 0.39$, $\alpha = 0.30$, and $n = 3.0 \times 10^{-4}$ for the equivalence ratio and $l = 0.27$, $\alpha = 0.55$, and $n = 1.3 \times 10^{-4}$ for the ammonia fraction.

To further assess the robustness of the GPR algorithm, the optimal hyperparameters were identified for 100 different training dataset seed numbers. Statistics are shown in Table 4. It is challenging to qualify if the COVs reported in Table 4 are *small* or *large*. However, given the sensitivity of the GPR algorithm to its hyperparameters for the data at hand, these variations were found to be small enough that it can be concluded that the regression performance is not very sensitive to the choice of the training dataset. To illustrate, training with the reference dataset (the one used for Fig. 6 and Table 3) using the hyperparameters that are the furthest away from those optimized for this dataset leads to coefficients of regression that remain large, namely $R^2 = 0.977$ for the equivalence ratio and $R^2 = 0.985$ for the ammonia fraction. This confirms that the GPR algorithm is robust because its performance is not very sensitive to the choice of the training dataset and hyperparameters.

### 3.3. Test of the GPR algorithm with turbulent swirl flames

So far, the GPR algorithm was only trained and validated with laminar flame data and it is important to test if it generalizes to new data, not included in the database from Zhu et al. [32]. This is also an opportunity to challenge predictions of equivalence ratio and ammonia fraction for more practical flames; in this case the premixed, turbulent swirl, ammonia-methane-air flames described in Section 2. Measurements in the laminar flames [32] and in the turbulent swirl flames were made with different spectrometers, featuring different spectral resolutions and sensitivities. Therefore, a 1-point calibration procedure was required to ensure that the turbulent swirl flame data were compatible with the GPR algorithm trained with laminar flame data. This was achieved by multiplying each X*/OH* ratio by a constant to ensure that this ratio was strictly the same for laminar flames and for turbulent swirl flames for one arbitrary operating condition, namely $\phi = 1.0$ and $X_{NH3} = 0.50$. These constants were 1.89, 1.17, and 1.17 for NH*/OH*, CN*/OH*, and CH*/OH* ratios, respectively. Note that this 1-point calibration procedure would not have been needed if laminar flames and turbulent swirl flames measurements had been conducted with the same optical setup.

Fig. 8 shows the prediction by the GPR algorithm for the 29 data

**Table 4**
Mean, coefficient of variation (COV), minimum, and maximum values of the hyperparameters optimized for 100 different training datasets if NO* and $CO_2$* are excluded from the inputs (i.e., inputs are NH*/OH*, CN*/OH*, and CH*/OH*).

| | | Mean | COV | Min | Max |
|---|---|---|---|---|---|
| $\phi$ | $l$ | 0.31 | 8% | 0.26 | 0.39 |
| | $\alpha$ | 0.50 | 25% | 0.25 | 0.98 |
| | $n$ | $1.9 \times 10^{-4}$ | 21% | $1.1 \times 10^{-4}$ | $4.1 \times 10^{-4}$ |
| $X_{NH3}$ | $l$ | 0.25 | 9% | 0.21 | 0.33 |
| | $\alpha$ | 1.15 | 50% | 0.28 | 4.16 |
| | $n$ | $2.0 \times 10^{-4}$ | 22% | $1.2 \times 10^{-4}$ | $3.6 \times 10^{-4}$ |

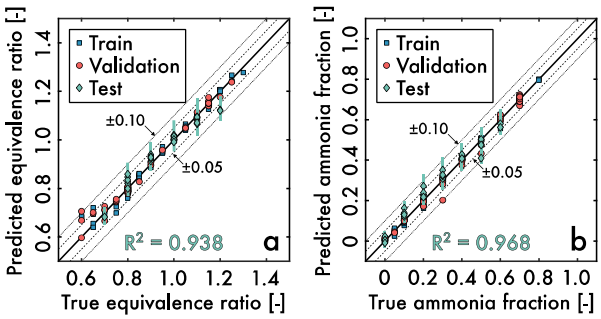


**Fig. 8.** Predicted equivalence ratio (a) and ammonia fraction (b) as a function of their true values for the training (blue squares), validation (red circles), and test (green diamonds, corresponding to the turbulent swirl flames) data points and for the optimum hyperparameters $l = 0.39$, $\alpha = 0.30$, and $n = 3.0 \times 10^{-4}$ (equivalence ratio) and $l = 0.27$, $\alpha = 0.55$, and $n = 1.3 \times 10^{-4}$ (ammonia fraction). The NO* and $CO_2$* excited radicals were excluded from the inputs (i.e., inputs are NH*/OH*, CN*/OH*, and CH*/OH*). Coefficients of determination in green correspond to the regressions on the test data points. Green vertical bars give the predictions' confidence intervals.

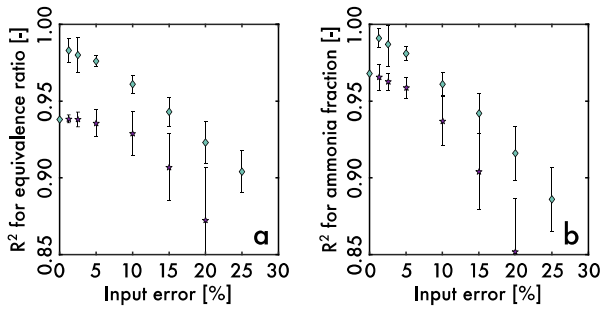


**Fig. 9.** Coefficients of determination of the regression on the test data points (corresponding to the turbulent swirl flames) as a function of the input error introduced in the training and validation datasets. Green diamonds correspond to cases where input error was only introduced in the laminar flames data. Purple stars are for cases where input error was also added to the turbulent swirl flames data.

points measured in the swirl flames, known as the *test* data points. Excited radicals NO* and $CO_2$* were excluded from the inputs and the hyperparameters were $l = 0.39$, $\alpha = 0.30$, and $n = 3.0 \times 10^{-4}$ for the equivalence ratio and $l = 0.27$, $\alpha = 0.55$, and $n = 1.3 \times 10^{-4}$ for the ammonia fraction, just as for Fig. 6 and Table 3. Fig. 8 also shows the training and validation data points corresponding to the laminar flames. The predictions of the equivalence ratio and ammonia fraction were successful for the test data points of the turbulent swirl flames, with regression coefficients $R^2 = 0.938$ for the equivalence ratio and $R^2 = 0.968$ for the ammonia fraction. Given the different spans of equivalence ratio and ammonia fraction considered in the laminar flames and in the turbulent swirl flames datasets, it is risky to compare the coefficients of regression directly. However, Fig. 8 also includes ±0.05 (dashed) and ±0.10 (dotted) lines that help quantify prediction errors. Both for the equivalence ratio and for the ammonia fraction, prediction errors are well below ±0.05 for the vast majority of data points, and errors are always below ±0.10. In addition, the true equivalence ratios and ammonia fractions are always located within the confidence intervals of the GPR algorithm's predictions (green vertical bars in Fig. 8) that could be estimated thanks to its probabilistic nature (cf. supplementary material for more details). Note that this arguably good performance was achieved for wide ranges of equivalence ratio ($0.80 \leq \phi \leq 1.20$) and ammonia fraction ($0 \leq X_{NH3} \leq 0.60$). Adding NO*/OH* and $CO_2$*/OH* ratios to the inputs worsened the predictions' performance, which is attributed to the rather high level of noise observed in the NO* spectral range, where the bench spectrometer is least sensitive.

### 3.4. Robustness of the GPR algorithm to measurement errors

The start-of-the-art spectroscopic hardware and the well-behaved nature of the steady laminar flames considered by Zhu et al. [32] led to measurement uncertainties that are likely to be well below what would be achieved in the field for more practical flames. This is why a less costly and more robust bench spectrometer and turbulent swirl flames were also considered in the present study. To further quantify the robustness of the GPR algorithm to measurement errors, the training and validation procedures were repeated after a random input error was introduced into the laminar flame data. The corresponding coefficients of determination for the predictions of equivalence ratio and ammonia fraction with the turbulent swirl flames' test dataset are shown in Fig. 9 (green diamonds) as a function of the input error. An input error of X% means that the NH*/OH*, CN*/OH*, and CH*/OH* ratios of the training and validation datasets were each multiplied by a different random number between 1 and $1 \pm X/100$. Due to the random nature of this error, each case was repeated many times, until convergence of the mean and rms coefficient of determination was achieved, and the variations are reflected with error bars. Hyperparameters were re-optimized for each test.

Fig. 9 shows that equivalence ratio predictions are fairly robust to measurement errors because the mean coefficient of determination remains above 0.90 even for input errors of ±25%, which is arguably larger than typical chemiluminescence measurement errors. Interestingly, the mean coefficient of determination is slightly higher if an input error between ±1.25% and ±15% is added compared to no input error at all. This behavior was not thoroughly investigated but is consistent with previous findings showing that noise injection can lead machine learning algorithms to be more robust to generalization [55]. In an extension of this work, retraining on a more diverse dataset could therefore potentially modify this behavior.

Fig. 9 shows that ammonia fraction predictions are also robust to measurement errors because the mean coefficient of determination only drops below 0.90 for ±25% of input errors or more. The mean coefficient of determination is slightly larger if an input error between ±1.25% and ±5% is added compared to no input error at all.

To quantify the robustness of GPR to measurement errors that could also be present in the test dataset, the same exercise was repeated but with random error added to the turbulent swirl flame data in addition to the laminar flame data. The results are shown in Fig. 9 as purple stars. For both the equivalence ratio and ammonia fraction predictions, the mean coefficient of determination decreases when the input error is increased above some threshold. Also consistent with expectations, for any given input error, the mean coefficient of determination is smaller when an error is added to the test dataset than when no error is added to this dataset. For equivalence ratio and ammonia fraction predictions, the mean coefficient of determination drops below 0.90 for more than ±15% of input error. Given the magnitude of measurement errors typically found in chemiluminescence measurements, the GPR can arguably be labeled as robust to errors in the turbulent swirl flame measurements.

### 3.5. Benchmark of the GPR algorithm against conventional methods

The machine learning-based GPR algorithm is only useful if its predictions outperform those obtained with existing methods. In this section, the GPR algorithm is first benchmarked against the more conventional, ratio-based method to monitor metrics in flames using chemiluminescence. Zhu et al. [32] identified that the CN*/NO* ratio is a suitable surrogate for the equivalence ratio in ammonia-methane-air flames because it is very sensitive to the equivalence ratio, while being somewhat insensitive to the ammonia fraction. This is shown in Fig. 10a, which plots the measured CN*/NO* ratio as a function of the

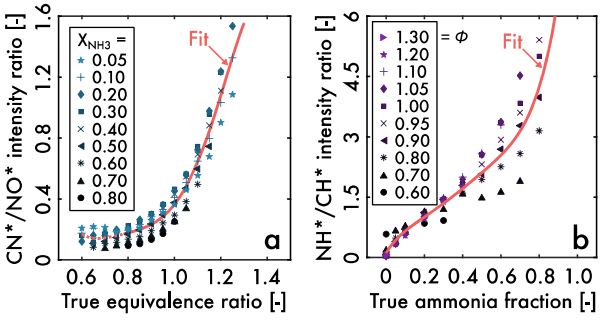


**Fig. 10.** CN*/NO* (a) and NH*/CH* (b) ratios as a function of the equivalence ratio and the ammonia fraction, respectively, measured in the laminar flames by Zhu et al. [32]. Solid red curves are 5th order polynomial fits.

equivalence ratio for different ammonia fractions for the laminar flames of Zhu et al. [32]. While an overall trend is apparent, there is some scatter in the data and a fit must be performed to obtain a calibration curve that can then be used to infer the equivalence ratio using CN*/NO* ratio measurements. This fit (5th-order polynomial) is shown as a solid red line in Fig. 10a.

Zhu et al. [32] also identified that the NH*/CH* ratio is a suitable surrogate for the ammonia fraction because it is very sensitive to it and much less to the equivalence ratio. Fig. 10b plots the measured NH*/CH* ratio as a function of the ammonia fraction for different equivalence ratios for the same laminar flames. There is also some scatter in the data and a fit must be done to obtain the calibration curve needed to infer the ammonia fraction using NH*/CH* ratio measurements.

Fig. 11 shows the equivalence ratios and ammonia fractions obtained using the calibration curves fitted in Fig. 10 and the CN*/NO* and NH*/CH* ratios measured in the laminar flames (red circles). The scatter and regression coefficients are much worse than those obtained with GPR trained with NH*/OH*, CN*/OH*, and CH*/OH* ratios as inputs and shown in Fig. 8 (blue squares and red circles). Most predictions feature discrepancies below ±0.15 but discrepancies of up to ±0.25 are seen, which is much more than ±0.05 and ±0.10, respectively, in Fig. 8. In addition, equivalence ratios $0.60 \leq \phi < 0.75$ cannot be measured with this ratio-based method because the calibration curve is not monotonic in this range. Fig. 11 also shows the equivalence ratios and ammonia fractions predicted for the turbulent swirl flames (green diamonds) by using the calibration curves fitted in Fig. 10. Discrepancies are up to 0.15 for both the equivalence ratio and the ammonia fraction, which is again worse than the scatter found for the GPR algorithm in Fig. 8 (green diamonds). To illustrate, the regression coefficient falls from $R^2 = 0.938$ to 0.555 for the equivalence ratio and from $R^2 = 0.968$ to 0.839 for the ammonia fraction.

Clearly, the performance of the ratio-based method is poorer than that of GPR trained with the best inputs, namely NH*/OH*, CN*/OH*, and CH*/OH* ratios (see Fig. 8). However, equivalence ratio predictions if only the CN*/NO* ratio is used as input of the GPR algorithm (not shown here) do not outperform the conventional ratio-based method highlighted in Fig. 11a. Similarly, the performance of ammonia fraction predictions is very close for the GPR trained only with the NH*/CH* and for the conventional ratio-based method highlighted in Fig. 11b. Consequently, the insufficient performance of the ratio-based method is due to the lack of chemical information coded into only one excited species ratio, and resorting to the more advanced GPR is not useful if no additional chemiluminescent inputs are provided.

It is also relevant to compare the performance of GPR to that of linear regression using the same chemiluminescent inputs, namely OH*, NH*, CN*, and CH*. A least square linear regression approach applied to the laminar flame dataset yields the following equations to predict the equivalence ratio and the ammonia fraction:

$$\phi = 0.15\frac{NH*}{OH*} + 0.41\frac{CN*}{OH*} + 1.55\frac{CH*}{OH*} + 0.66 \quad (3)$$

$$X_{NH3} = 2.63\frac{NH*}{OH*} - 2.35\frac{CN*}{OH*} + 0.06\frac{CH*}{OH*} + 0.11 \quad (4)$$

Fig. 12 shows the equivalence ratios and ammonia fractions predicted using Eqs. (3) and (4). The scatter and regression coefficients are much worse than those obtained with the GPR algorithm in Fig. 8, for both the laminar flames and the turbulent swirl flames. For the latter, discrepancies are up to 0.15 for the equivalence ratio and the ammonia fraction.

Examination of Fig. 1 indicates that the problem at hand is intrinsically non-linear, implying that the poor prediction performance of a linear regression should not come as a surprise. Therefore, it is useful to assess the performance of higher order polynomial fits. With scikit-learn's toolbox, a $n^{th}$ order polynomial fit is most conveniently achieved by taking the linear regression of inputs that were previously extended to include their exponents (from 1 to n) as well as their cross products featuring an order smaller than or equal to n. For example, with NH*/OH*, CN*/OH*, and CH*/OH* as the three "original" inputs, a 2nd order polynomial fit would require 10 coefficients to fit the following inputs: [1, NH*/OH*, CN*/OH*, CH*/OH*, NH*/OH* × CN*/OH*, NH*/OH* × CH*/OH*, CN*/OH* × CH*/OH*, $(NH*/OH*)^2$, $(CN*/OH*)^2$, $(CH*/OH*)^2$].

For a fair comparison with GPR that features optimum hyperparameters that are a priori unknown, the optimal order of the polynomial should be treated as a hyperparameter too, and it should be identified through the same train/validation exercise and datasets. For the herein data, a 4th order polynomial (35 coefficients) yielded the best regression coefficients on the validation datapoints, specifically $R^2 = 0.983$ and 0.986 for the equivalence ratio and ammonia fraction, respectively. Fig. 13 shows the equivalence ratios and ammonia fractions predicted with 4th order polynomial fits for the laminar flames

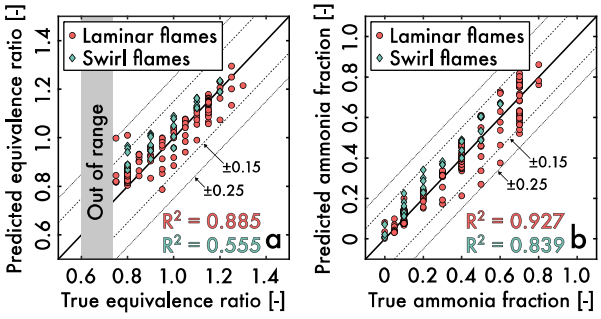


**Fig. 11.** Predicted equivalence ratio (a) and ammonia fraction (b) as a function of their true values for the laminar flames (red circles) and turbulent swirl flames (green diamonds) using the ratio-based method (i.e., inputs are CN*/NO* or NH*/CH*) with the calibration curves fitted in Fig. 10.

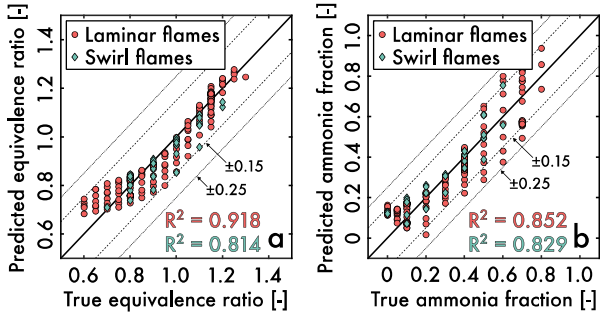


**Fig. 12.** Predicted equivalence ratio (a) and ammonia fraction (b) as a function of their true values for the laminar flames (red circles) and turbulent swirl flames (green diamonds) using linear regression (see Eqs. (3) and (4)) of the laminar flames data (inputs are NH*/OH*, CN*/OH*, and CH*/OH*).

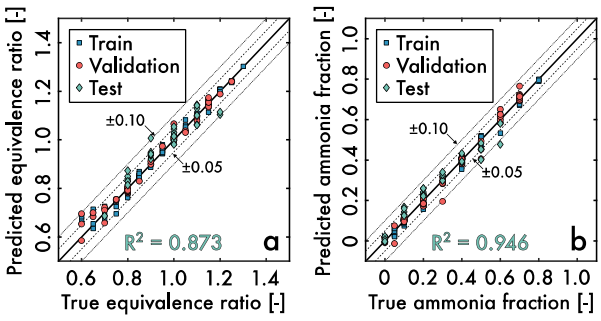


**Fig. 13.** Predicted equivalence ratio (a) and ammonia fraction (b) as a function of their true values for the training (blue squares), validation (red circles), and test (green diamonds, corresponding to the turbulent swirl flames) data points using a 4th order polynomial regression (inputs are NH*/OH*, CN*/OH*, and CH*/OH*). Coefficients of determination in green correspond to the regressions on the test data points.

(validation datapoints in red) and turbulent swirl flames (test datapoints in green). Fig. 13 should be compared to Fig. 8 which shows the performance of GPR trained with the exact same dataset. Overall, while the prediction performance of the 4th order polynomial fits is good (prediction errors are within 5% for most datapoints), regression coefficients are smaller for the 4th order polynomial fits ($R^2 = 0.873$ and 0.946) than for the GPR ($R^2 = 0.938$ and 0.968). More important, inherent in the method, predictions made using the 4th order polynomial fits cannot be provided with a confidence interval while such a confidence interval is an output of GPR. This confirms that resorting to the more advanced GPR is worth the effort for predictions of equivalence ratio and ammonia fraction in premixed ammonia-methane-air flames.

### 3.6. Future steps

Data showed that knowledge of the chemiluminescence intensities of the OH*, NH*, CN*, and CH* excited radicals is sufficient to infer the equivalence ratio and the ammonia fraction of premixed ammonia-methane-air flames. This is useful to develop optical sensors for the monitoring of such flames because the important spectral features are now clearly identified. However, previous studies [47,48] have shown that *a priori* identification of these spectral features is not necessary, at least for methane-air and methane-hydrogen-air flames, because these can be extracted automatically using advanced methods, such as POD, if a sufficiently broadband chemiluminescence spectrum is available. Arguably, such advanced methods will be challenging to implement in future practical flames, which may not be perfectly premixed. Recent studies suggested that stratified ammonia-methane-air or ammonia-hydrogen-air flames, i.e., flames featuring a spatially-varying equivalence ratio [1,56,57] and/or ammonia fraction [56,57], could be used instead of premixed flames to promote flame stabilization, control NOx emissions, and mitigate thermoacoustic coupling. In such flames, simultaneous, local measurement of the broadband chemiluminescence spectrum at multiple flame locations would be required, which is not possible to achieve with a conventional spectrometer paired with a CCD/CMOS sensor. Alternatively, OH*, NH*, CN*, and CH* chemiluminescence intensities may be recorded on four separate CCD/CMOS cameras, each equipped with the appropriate bandpass filter. Note that the line-of-sight nature of chemiluminescence implies that it should be recorded from multiple viewpoints so that a tomographic reconstruction [58] could be applied before using the GPR algorithm. To the best of the authors' knowledge, simultaneous tomographic reconstruction of four excited radicals has never been achieved before but, in principle, combining the ingredients of tomographic reconstruction [58] with those of multi-species imaging recently demonstrated in [59] could work. This is the topic of a future study.

The method described in this study, as well as future spatially resolved measurements based on tomographic reconstruction, rely strongly on the fact that chemiluminescence intensities are spatially integrated over the whole flame coordinate (also referred to as flame normal) for each of the excited radicals. This is an important characteristic of the method implying that the flame front itself cannot be spatially resolved along its normal. This is because the shape and location of concentration profiles across the flame are different for each excited radical. Indeed, chemical reactions responsible for the formation and consumption of each excited radical are different and are active at different locations across the flame. Consequently, chemiluminescence ratios are expected to vary across the flame front, which is not compatible with the herein method where each flame is defined by a single number for the chemiluminescence intensity of each excited radical. Therefore, for the method to succeed, the probe volume over which chemiluminescence intensities are measured must be substantially larger than the flame thickness, often in the order of a few millimeters or less. The size of the probe volume would then dictate the actual spatial resolution of equivalence ratio and ammonia fraction measurements. Note that equivalence ratio and ammonia fraction are global properties of premixed flamelets, meaning that it is not physically meaningful to define them as a function of the flame coordinate/normal (i.e., each premixed flamelet can be defined by a unique equivalence ratio and a unique ammonia fraction). Consequently, the fact that the herein method must spatially integrate chemiluminescence intensities across the whole flame coordinate/normal is not a significant limitation. However, if chemiluminescence data from laminar flames are used to train the GPR algorithm, application of the method must be limited to turbulent flames belonging to the flamelet region of the premixed turbulent combustion regime diagram. Flamelets (either wrinkled or corrugated) are flame sheets that locally retain the structure of laminar flames. Such flames are largely represented in lab- or practical-scale flames. For turbulent flames belonging to the thin reaction zone or broken reaction zone regions of the regime diagram, i.e., those subjected to much more extreme levels of turbulence, the applicability of the herein method is not guaranteed and should be verified.

## 4. Conclusion

This study reported on the development and benchmarking of a chemiluminescence- and machine learning-based method to measure the equivalence ratio and the ammonia fraction in premixed ammonia-methane-air flames. To predict these key flame metrics, a Gaussian process regression (GPR) algorithm was trained using only chemiluminescence data previously recorded in laminar flames. The algorithm was then challenged using input data from more practical, turbulent swirl flames. The key findings were as follows:

- Using the ratios NH*/OH*, CN*/OH*, and CH*/OH* as inputs is sufficient to train the GPR algorithm to accurately predict the equivalence ratio and the ammonia fraction in both laminar and turbulent flames.
- Prediction errors on the equivalence ratio and ammonia fraction are generally smaller than 0.05 and extend to a maximum of 0.10 for a very small subset of operating conditions. This performance was achieved for large ranges of equivalence ratio ($0.60 \leq \phi \leq 1.30$ for the laminar flames and $0.80 \leq \phi \leq 1.20$ for the turbulent flames) and ammonia fraction ($0 \leq X_{NH3} \leq 0.80$ for the laminar flames and $0 \leq X_{NH3} \leq 0.60$ for the turbulent flames).
- The GPR algorithm was also trained after adding NO* and $CO_2$* to the list of excited radicals, but this did not improve predictions.
- The performance of the GPR algorithm was compared to that of linear regression and a more conventional, ratio-based method relying only on CN*/NO* and NH*/CH* ratios. The prediction errors on the equivalence ratio and the ammonia fraction were often larger than 0.15 with this ratio-based method, which is significantly worse than that of GPR when trained with the best combination of excited

radicals. However, GPR did not overperform the ratio-based method when its training was restricted to the same excited radicals (CN*/NO* or NH*/CH*).

- The GPR algorithm also significantly outperformed linear regression. However, 4th order polynomial fits achieved a prediction performance almost as good as GPR. Nevertheless, GPR provides a confidence interval for its prediction, which a 4th order polynomial fit cannot do. Given that GPR and 4th order polynomial fit are both equally straightforward to implement with scikit-learn, GPR should be favored.

This work lays strong foundations for the development of non-intrusive sensors to monitor practical, premixed ammonia-methane-air flames. This could be extended in the future to stratified flames through additional advances in spatially resolved, multi-species imaging.

## Declaration of Competing Interest

The authors declare that they have no known competing financial interests or personal relationships that could have appeared to influence the work reported in this paper.

## Data availability

Data and code have been shared as supplementary materials

## Acknowledgments

This research was supported by funding from the King Abdullah University of Science and Technology (KAUST) (BAS/1/1425–01–01).

## Supplementary materials

Supplementary material associated with this article can be found, in the online version, at doi:10.1016/j.jaecs.2023.100212.

## References

[1] Kobayashi H, Hayakawa A, Somarathne KDKA, Okafor EC. Science and technology of ammonia combustion. Proc Combust Inst 2019;37:109–33. https://doi.org/10.1016/j.proci.2018.09.029.

[2] Valera-Medina A, Xiao H, Owen-Jones M, David WIF, Bowen PJ. Ammonia for power. Prog Energy Combust Sci 2018;69:63–102. https://doi.org/10.1016/j.pecs.2018.07.001.

[3] Valera-Medina A, Amer-Hatem F, Azad AK, Dedoussi IC, de Joannon M, Fernandes RX, Glarborg P, Hashemi H, He X, Mashruk S, McGowan J, Mounaim-Rouselle C, Ortiz-Prado A, Ortiz-Valera A, Rossetti I, Shu B, Yehia M, Xiao H, Costa M. Review on ammonia as a potential fuel: From synthesis to economics. Energy Fuels 2021;35:6964–7029. https://doi.org/10.1021/acs.energyfuels.0c03685.

[4] Elbaz AM, Wang S, Guiberti TF, Roberts WL. Review on the recent advances on ammonia combustion from the fundamentals to the applications. Fuel Comms 2022;10:100053. https://doi.org/10.1016/j.jfueco.2022.100053.

[5] Chiong MC, Chong CT, Ng JH, Mashruk S, Chong WWF, Samiran NA, Mong GR, Valera-Medina A. Advancements of combustion technologies in the ammonia-fuelled engines. Energy Convers Manag 2021;244:114460. https://doi.org/10.1016/j.enconman.2021.114460.

[6] Lee H, Lee MJ. Recent advances in ammonia combustion technology in thermal power generation system for carbon emission reduction. Energies 2021;14:5604. https://doi.org/10.3390/en14185604.

[7] Kurata O, Iki N, Matsunuma T, Inoue T, Tsujimura T, Furutani H, Kobayashi H, Hayakawa A. Performances and emission characteristics of $NH_3$–air and $NH_3$–$CH_4$–air combustion gas-turbine power generations. Proc Combust Inst 2017;36:3351–9. https://doi.org/10.1016/j.proci.2016.07.088.

[8] Ávila CD, Cardona S, Abdullah M, Younes M, Jamal A, Guiberti TF, Roberts WL. Experimental assessment of the performance of a commercial micro gas turbine fueled by ammonia-methane blends. Appl Energ Combust Sci 2023;13:100104. https://doi.org/10.1016/j.jaecs.2022.100104.

[9] Tamura M, Gotou T, Ishii H, Riechelmann D. Experimental investigation of ammonia combustion in a bench scale 1.2 MW-thermal pulverised coal firing furnace. Appl Energy 2020;277:115580. https://doi.org/10.1016/j.apenergy.2020.115580.

[10] Zhang M, An Z, Wei X, Wang J, Huang Z, Tan H. Emission analysis of the $CH_4$/$NH_3$/air co-firing fuels in a model combustor. Fuel 2021;291:120135. https://doi.org/10.1016/j.fuel.2021.120135.

[11] Okafor EC, Somarathne KDKA, Ratthanan R, Hayakawa A, Kudo T, Kurata O, Iki N, Tsujimura T, Furutani H, Kobayashi H. Control of NOx and other emissions in micro gas turbine combustors fuelled with mixtures of methane and ammonia. Combust Flame 2020;211:406–16. https://doi.org/10.1016/j.combustflame.2019.10.012.

[12] Jójka J, Ślefarski R. Emission characteristics for swirl methane–air premixed flames with ammonia addition. Energies 2021;14:602. https://doi.org/10.3390/en14030662.

[13] Khateeb AA, Guiberti TF, Wang G, Boyette WR, Younes M, Jamal A, Roberts WL. Stability limits and NO emissions of premixed swirl ammonia-air flames enriched with hydrogen or methane at elevated pressures. Int J Hydrogen Energ 2021;46:11969–81. https://doi.org/10.1016/j.ijhydene.2021.01.036.

[14] Zhang M, Wei X, Wang J, Huang Z, Tan H. The blow-off and transient characteristics of co-firing ammonia/methane fuels in a swirl combustor. Proc Combust Inst 2021;38:5181–90. https://doi.org/10.1016/j.proci.2020.08.056.

[15] Ayaz SK, Altuntas O, Caliskan H. Thermoecologic assessment and life cycle–based environmental pollution cost analysis of microgas turbine. J Environ Eng 2020;146:04019096. https://doi.org/10.1061/(ASCE)EE.1943-7870.0001611.

[16] Somarathne KDKA, Okafor EC, Sugawara D, Hayakawa A, Kobayashi H. Effects of OH concentration and temperature on NO emission characteristics of turbulent non-premixed $CH_4$/$NH_3$/air flames in a two-stage gas turbine like combustor at high pressure. Proc Combust Inst 2021;38:5163–70. https://doi.org/10.1016/j.proci.2020.06.276.

[17] Khateeb AA, Guiberti TF, Zhu X, Younes M, Jamal A, Roberts WL. Stability limits and exhaust NO performances of ammonia-methane-air swirl flames. Exp Therm Fluid Sci 2020;114:110058. https://doi.org/10.1016/j.expthermflusci.2020.110058.

[18] Xiao H, Valera-Medina A, Bowen PJ. Study on premixed combustion characteristics of co-firing ammonia/methane fuels. Energy 2017;140:125–35. https://doi.org/10.1016/j.energy.2017.08.077.

[19] Hayakawa A, Goto T, Mimoto R, Kudo T, Kobayashi H. NO formation/reduction mechanisms of ammonia/air premixed flames at various equivalence ratios and pressures. Mech Eng J 2015;2:14–00402. https://doi.org/10.1299/mej.14-00402.

[20] Okafor EC, Naito Y, Colson S, Ichikawa A, Kudo T, Hayakawa A, Kobayashi H. Experimental and numerical study of the laminar burning velocity of $CH_4$–$NH_3$–air premixed flames. Combust Flame 2018;187:185–98. https://doi.org/10.1016/j.combustflame.2017.09.002.

[21] Miller JA, Smooke MD, Green RM, Kee RJ. Kinetic modeling of the oxidation of ammonia in flames. Combust Sci Technol 1983;34:149–76. https://doi.org/10.1080/00102208308923691.

[22] Glarborg P, Miller JA, Ruscic B, Klippenstein SJ. Modeling nitrogen chemistry in combustion. Prog Energy Combust Sci 2018;67:31–68. https://doi.org/10.1016/j.pecs.2018.01.002.

[23] Hardalupas Y, Orain M. Local measurements of the time-dependent heat release rate and equivalence ratio using chemiluminescent emission from a flame. Combust Flame 2004;139:188–207. https://doi.org/10.1016/j.combustflame.2004.08.003.

[24] Ikeda Y, Kojima J, Hashimoto H. Local chemiluminescence spectra measurements in a high-pressure laminar methane/air premixed flame. Proc Combust Inst 2002;29:1495–501. https://doi.org/10.1016/S1540-7489(02)80183-3.

[25] Cheng TS, Wu CY, Li YH, Chao YC. Chemiluminescence measurements of local equivalence ratio in a partially premixed flame. Combust Sci Technol 2006;178:1821–41. https://doi.org/10.1080/00102200600790755.

[26] Panoutsos CS, Hardalupas Y, Taylor AMKP. Numerical evaluation of equivalence ratio measurement using OH* and CH* chemiluminescence in premixed and non-premixed methane–air flames. Combust Flame 2009;156:273–91. https://doi.org/10.1016/j.combustflame.2008.11.008.

[27] Hardalupas Y, Panoutsos CS, Taylor AMKP. Spatial resolution of a chemiluminescence sensor for local heat-release rate and equivalence ratio measurements in a model gas turbine combustor. Exp Fluids 2010;49:883–909. https://doi.org/10.1007/s00348-010-0915-z.

[28] Ballester J, García-Armingol T. Diagnostic techniques for the monitoring and control of practical flames. Prog Energy Combust Sci 2010;411:375–411. https://doi.org/10.1016/j.pecs.2009.11.005.

[29] Guiberti TF, Durox D, Schuller T. Flame chemiluminescence from $CO_2$- and $N_2$-diluted laminar $CH_4$/air premixed flames. Combust Flame 2017;181:110–22. https://doi.org/10.1016/j.combustflame.2017.01.032.

[30] Quintino FM, Trindade TP, Fernandes EC. Biogas combustion: Chemiluminescence fingerprint. Fuel 2018;231:328–40. https://doi.org/10.1016/j.fuel.2018.05.086.

[31] Leipertz A, Obertacke R, Wintrich F. Industrial combustion control using UV emission tomography. Symp (Int) Combust 1996;26:2869–75. https://doi.org/10.1016/S0082-0784(96)80127-5.

[32] Zhu X, Khateeb AA, Roberts WL, Guiberti TF. Chemiluminescence signature of premixed ammonia-methane-air flames. Combust Flame 2021;231:111508. https://doi.org/10.1016/j.combustflame.2021.111508.

[33] Fowler A, Badami JS. The spectrum of the hydrogen-nitrous oxide flame. Proc R Soc Lond A 1931;133:325–32. https://doi.org/10.1098/rspa.1931.0151.

[34] Wolfhard HG, Parker WG. A spectroscopic investigation into the structure of diffusion flames. Proc Phys Soc, A 1952;65:2–19. https://doi.org/10.1088/0370-1298/65/1/302.

[35] Farber M, Darnell AJ. Spectroscopic examination of the $NH_3$–$HNO_3$ and NH–$NO_2$ diffusion flames. J Chem Phys 1954;22:1261–3. https://doi.org/10.1063/1.1740357.

[36] Kaskan WE, Hughes DE. Mechanism of decay of ammonia in flame gases from an $NH_3/O_2$ flame. Combust Flame 1973;20:381–8. https://doi.org/10.1016/0010-2180(73)90030-8.
[37] Gaydon A. The spectroscopy of flames. 2nd ed. Netherlands: Springer; 1974.
[38] Zhang D, Gao Q, Li B, Liu J, Tian Y, Li Z. Femtosecond laser-induced plasma spectroscopy for combustion diagnostics in premixed ammonia/air flames. Appl Opt 2019;58:7810–6. https://doi.org/10.1364/AO.58.007810.
[39] Pugh D, Runyon J, Bowen P, Giles A, Valera-Medina A, Marsh R, Goktepe B, Hewlett S. An investigation of ammonia primary flame combustor concepts for emissions reduction with OH*, $NH_2$* and NH* chemiluminescence at elevated conditions. Proc Combust Inst 2021;38:6451–9. https://doi.org/10.1016/j.proci.2020.06.310.
[40] Zhu X, Khateeb AA, Guiberti TF, Roberts WL. NO and OH* emission characteristics of very-lean to stoichiometric ammonia–hydrogen–air swirl flames. Proc Combust Inst 2021;38:5155–62. https://doi.org/10.1016/j.proci.2020.06.275.
[41] Ku JW, Choi S, Kim HK, Lee S, Kwon OC. Extinction limits and structure of counterflow nonpremixed methane-ammonia/air flames. Energy 2018;165:314–25. https://doi.org/10.1016/j.energy.2018.09.113.
[42] Zhu X, Roberts WL, Guiberti TF. UV-visible chemiluminescence signature of laminar ammonia-hydrogen-air flames. Proc Combust Inst 2022. https://doi.org/10.1016/j.proci.2022.07.021. press.
[43] Mashruk S, Zhu X, Roberts WL, Guiberti TF, Valera-Medina A. Chemiluminescent footprint of premixed ammonia-methane-air swirling flames. Proc Combust Inst 2022. https://doi.org/10.1016/j.proci.2022.08.073. press.
[44] Weng W, Aldén M, Li Z. Visible chemiluminescence of ammonia premixed flames and its application for flame diagnostics. Proc Combust Inst 2022. https://doi.org/10.1016/j.proci.2022.08.012. press.
[45] Ballester J, Hernández R, Sanz A, Smolarz A, Barroso J, Pina A. Chemiluminescence monitoring in premixed flames of natural gas and its blends with hydrogen. Proc Combust Inst 2009;32:2983–91. https://doi.org/10.1016/j.proci.2008.07.029.
[46] Tripathi MM, Krishnan SR, Srinivasan KK, Yueh FY, Singh JP. Chemiluminescence-based multivariate sensing of local equivalence ratios in premixed atmospheric methane–air flames. Fuel 2012;93:684–91. https://doi.org/10.1016/j.fuel.2011.08.038.
[47] Yoon T, Y-e Kang, Kim SW, Park Y, Yee K, Carter CD, Hammack SD, Do H. Proper orthogonal decomposition of continuum-dominated emission spectra for simultaneous multi-property measurements. Energy 2022;254:124458. https://doi.org/10.1016/j.energy.2022.124458.
[48] Lee J, McGann B, Hammack SD, Carter C, Lee T, Do H, Bak MS. Machine learning based quantification of fuel-air equivalence ratio and pressure from laser-induced plasma spectroscopy. Opt Express 2021;29:17902–14. https://doi.org/10.1364/OE.425096.
[49] Rasmussen CE, Williams CKI. Gaussian processes for machine learning. Cambridge, MA: MIT Press; 2006.
[50] Pedregosa F, Varoquaux G, Gramfort A, Michel V, Thirion B, Grisel O, Blondel M, Prettenhofer P, Weiss R, Dubourg V, Vanderplas J, Passos A, Cournapeau D, Brucher M, Perrot M, Duchesnay É. Scikit-learn: Machine Learning in Python. J Mach Learn Res 2011;12:2815–30.
[51] scikit-learn.org. Gaussian processes on scikit-learn, https://scikit-learn.org/stable/modules/gaussian_process.html#gaussian-processes; 2007 [accessed 19 January 2023].
[52] Palies P, Durox D, Schuller T, Candel S. The combined dynamics of swirler and turbulent premixed swirling flames. Combust Flame 2010;157:1698–717. https://doi.org/10.1016/j.combustflame.2010.02.011.
[53] Guiberti TF, Durox D, Zimmer L, Schuller T. Analysis of topology transitions of swirl flames interacting with the combustor side wall. Combust Flame 2015;162:4342–57. https://doi.org/10.1016/j.combustflame.2015.07.001.
[54] Di Sabatino F, Guiberti TF, Boyette WR, Roberts WL, Moeck JP, Lacoste DA. Effect of pressure on the transfer functions of premixed methane and propane swirl flames. Combust Flame 2018;193:272–82. https://doi.org/10.1016/j.combustflame.2018.03.011.
[55] Sietsma J, Dow RJF. Creating artificial neural networks that generalize. Neural Netw 1991;4:67–79. https://doi.org/10.1016/0893-6080(91)90033-2.
[56] Katoch A, Guiberti TF, de Campos DV, Lacoste DA. Dual-fuel, dual-swirl burner for the mitigation of thermoacoustic instabilities in turbulent ammonia-hydrogen flames. Combust Flame 2022;246:112392. https://doi.org/10.1016/j.combustflame.2022.112392.
[57] Elbaz AM, Albalawi AM, Wang S, Roberts WL. Stability and characteristics of $NH_3/CH_4$/air flames in a combustor fired by a double swirl stabilized burner. Proc Combust Inst 2022. https://doi.org/10.1016/j.proci.2022.06.004. press.
[58] Yu T, Li Z, Ruan C, Chen F, Lu X, Cai W. Development of an absorption-corrected method for 3D computed tomography of chemiluminescence. Meas Sci Technol 2019;30:045403. https://doi.org/10.1088/1361-6501/ab01c1.
[59] Guiberti TF, Krishna Y, Boyette WR, Yang C, Roberts WL, Magnotti G. Single-shot imaging of major species and OH mole fractions and temperature in non-premixed $H_2/N_2$ flames at elevated pressure. Proc Combust Inst 2021;38:1647–55. https://doi.org/10.1016/j.proci.2020.06.252.